Journal of Materials Chemistry A

ROYAL SOCIETY OF CHEMISTRY

PAPER

View Article Online
View Journal | View Issue

Cite this: J. Mater. Chem. A, 2022, 10, 19757

Electronic engineering of amorphous Fe–Co–S sites in hetero-nanoframes for oxygen evolution and flexible Al–air batteries†

Min Lu,[a] Li An,[a] Jie Yin,[a] Jing Jin,[a] Rui Yang,[a] Bolong Huang, *[b] Yang Hu,[a] Yong-Qing Zhao [a] and Pinxian Xi *[a]

Received 9th January 2022
Accepted 22nd February 2022

DOI: 10.1039/d2ta00191h

rsc.li/materials-a

The electrochemical oxygen evolution reaction (OER) and oxygen reduction reaction (ORR) are key electrochemical processes in metal–air batteries and water splitting devices. Aluminium–air batteries, as an important type of metal–air battery, have been considered to be promising power candidates for flexible electronics. Here, we describe electronically engineered amorphous Fe–Co–S sites embedded in Prussian blue analogue ($FeCoS_x$-PBA) hetero-nanoframes. The experimental results and DFT calculations reveal the critical role of the introduced $FeCoS_x$ layer to PBA, which enhances the electron transfer and alleviates the overbinding effect of OH* during the OER. The $FeCoS_x$-PBA hybrid system supplies an optimized electronic structure for the alkaline OER, which is also confirmed by the much-lowered overpotential (266 mV at 10 mA cm^{-2}) for the alkaline OER. Furthermore, a flexible Al–air battery based on an $FeCoS_x$-PBA cathode catalyst exhibits a high peak power density (58.3 mW cm^{-2}) and energy density (1483 W h kg_{Al}^{-1}), and outstanding stability for more than 50 h of operation under bending or stretching conditions, demonstrating its potential in the practical application of flexible electronic devices. Our results may provide a new strategy of modulating the electronic structure of air electrode catalysts to efficiently promote the reactivity of alkaline OER and Al–air battery processes.

Introduction

The rapid development of flexible and wearable electronic equipment is promoting the exploitation of highly efficient energy storage and conversion devices such as metal–air batteries. It has remarkable advantages of high theoretical energy density, excellent safety, and low cost compared to traditional batteries (such as lithium-ion batteries). The reaction involving oxygen is the most crucial process for metal–air batteries in portable devices and electric vehicles.[1–3] However, the related electro-process involving oxygen is usually restricted by the intrinsically sluggish kinetics for multiple-step proton-coupled electron transfer steps.[4,5] Therefore, developing highly efficient catalysts with excellent activity and predominant durability is critical for practical applications. Although noble metal and metal oxides (Pt, Ir, and IrO_2) exhibit state-of-the-art catalytic activities for the process involving oxygen, their multiple disadvantages, including high cost, scarcity, and poor durability, limit their application on a commercial scale.[6] For this purpose, the development of low-cost and highly active transition metal-based catalysts is essential.[7–9]

Hetero-nanoframes consisting of hollow frame structures have been considered an essential morphology in nanocatalysts due to their abundant exposed active sites, enhanced mass/charge transfer velocity, reduced possibility of aggregation, and favorable interface effects.[10–12] However, the poor intrinsic

[a]State Key Laboratory of Applied Organic Chemistry, Frontiers Science Center for Rare Isotopes, College of Chemistry and Chemical Engineering, Lanzhou University, Lanzhou, 730000, China. E-mail: xipx@lzu.edu.cn

[b]Department of Applied Biology and Chemical Technology, The Hong Kong Polytechnic University, Hung Hum, Kowloon, Hong Kong SAR, China. E-mail: bhuang@polyu.edu.hk

† Electronic supplementary information (ESI) available. See DOI: 10.1039/d2ta00191h

Pinxian Xi received his PhD degree in 2010 from Lanzhou University. From 2009 to 2010 he worked as a visiting scholar at Brown University. In 2018, he was appointed professor by the College of Chemistry and Chemical Engineering of Lanzhou University. His research focuses on the controlled synthesis of functional materials (including transition metal sulfide, rare earth functional materials) and developing their applications in the electrocatalytic and energy fields.

catalytic performance is still a challenge for their application in electrocatalysis. Cation and anion exchange is an efficient approach to modify the inherent electronic structure and create new active sites through the introduction of hetero-atoms, thus improving the intrinsic catalytic activity. After the introduction of heteroatoms, the surface electron density of active sites can be changed due to the variational coordination environment among neighboring atoms accompanied by the mismatch between electronegativity and ionic radius.[13] Accordingly, a tailored electronic configuration with an optimized band structure and abundant defects can be adjusted into catalysts through a precise ion-exchange strategy, which is favorable for promoting catalytic activity.[14–16]

In our work, an amorphous $FeCoS_x$ embedded in Prussian blue analogue hetero-nanoframes ($FeCoS_x$-PBA) was fabricated through an ultrasound-assisted ion-exchange method. By engineering the electronic structure through hetero-ion introduction (Fe^{2+} and S^{2-}) and amorphization, the $FeCoS_x$-PBA catalyst has enhanced electron transfer capability and optimized binding strength with intermediates. Besides, its unique hetero-nanoframe morphology also provides more exposed active sites. The as-obtained material exhibits an excellent oxygen evolution performance with a low overpotential of 266 mV at 10 mA cm^{-2} and superior durability. A dynamic OER study unravels the important role of S atoms in the OER with the $FeCoS_x$-PBA catalyst. Through DFT calculations, the obvious change in the electronic structures was unraveled, which indicates the boosted electronic conductivity to promote electron/charge transfer during the OER. Meanwhile, the surface-unsaturated $FeCoS_x$ layer demonstrates the optimized binding strength of OH, leading to the alleviated energy barrier of the rate-determining step for the OER. In addition, when serving as an air cathode catalyst in Al–air batteries, $FeCoS_x$-PBA shows enhanced battery performance. A remarkably high discharge power density of 58.3 mW cm^{-2}, a large energy density of 1483 W h kg^{-1} and excellent long-term stability for more than 50 h of operation after mechanical recharge were achieved. More importantly, all-solid-state Al–air batteries with excellent bendability and stretchability were assembled and applied to charge a smartphone successfully.

Experimental section

Materials and methods

Materials. $Co(NO_3)_2 \cdot 6H_2O$ (99.0%), $FeSO_4$ (99.0%), $K_3Fe(CN)_6$ (99.0%), sodium citrate (98.0%), thioacetamide (99.0%), ethanol (99.5%), $Na_2S \cdot 9H_2O$, and KOH (99.99%) were purchased from Aladdin. Deionized (DI) water was obtained from a Millipore Autopure system (18.2 MΩ, Millipore Ltd., USA). All the other materials for electrochemical measurements were of analytical grade and used without further purification.

Synthesis of PBA. The uniform PBA nanocubes were synthesized by a simple precipitation method. In a typical procedure, $Co(NO_3)_2 \cdot 6H_2O$ (6 mmol) and sodium citrate (9 mmol) were dissolved in deionized (DI) water (200 mL) to form solution A. At the same time, $K_3Fe(CN)_6$ (4 mmol) was dissolved in DI water (200 mL) to form solution B. Then, solutions A and B were mixed under magnetic stirring for 1 min. The obtained mixed solution was aged for 18 h at 30 °C. After collection by centrifugation and washing with water and ethanol, the precipitates were dried at 40 °C overnight[17–19]

Synthesis of MPBA. MPBA was synthesized in a cation exchange procedure. $FeSO_4$ (500 mg) was dissolved in 2 mol L^{-1} HCl solution (20 mL). Then PBA (50 mg) was added into the as-obtained solution, and treated ultrasonically for an hour at room temperature. The precipitate was collected by centrifugation, washed with water and ethanol and dried at 40 °C overnight.

Synthesis of $FeCoS_x$-PBA. MPBA powder (20 mg) was mixed with ethanol (20 mL) under ultrasonication for two hours. Then thioacetamide (50 mg) was dissolved in ethanol (10 mL) and added into the previous MPBA suspension under magnetic stirring for 30 minutes. The mixture was transferred into a 50 mL Teflon-lined stainless-steel autoclave and kept at 160 °C for 12 h in an electric oven. The final products were collected by centrifugation and washed with DI water and ethanol several times, before drying at 40 °C overnight.

Synthesis of $FeCoS_x$. MPBA powder (20 mg) was mixed with ethanol (20 mL) under ultrasonication for two hours. Then Na_2S (200 mg) was dissolved in H_2O (10 mL) and added into the previous MPBA suspension under magnetic stirring for 30 minutes. The mixture was transferred into a 50 mL Teflon-lined stainless-steel autoclave and kept at 160 °C for 12 h in an electric oven. The final products were collected by centrifugation and washed with DI water and ethanol several times, before drying at 40 °C overnight.

Structural characterizations

X-ray diffraction (XRD) experiments were conducted with an X'Pert Pro X-ray diffractometer with Cu Kα radiation ($\lambda = 0.1542$ nm) from 10° to 90° under a constant voltage of 40 kV. Field-emission scanning electron microscopy (FESEM) was used to investigate the morphologies of the samples at an accelerating voltage of 5 kV. Transmission electron microscopy (TEM) and high-resolution transmission electron microscopy (HRTEM) were performed under an acceleration voltage of 200 kV with a JEOL JEM 2100 TEM. X-ray photoelectron spectroscopy (XPS) analyses were undertaken with a VG ESCALAB 220I-XL device and corrected with the C 1s line at 284.8 eV. The Mössbauer spectrum was recorded in transmission mode with a ^{57}Co source in a rhodium matrix. The Mössbauer spectrometer was of the electromechanical type with a fixed absorber and operating source in constant acceleration mode, which was calibrated using an α-Fe foil. The Mössbauer spectrum was least-squares fitted, providing the values of the hyperfine field (H_{hf}), isomer shift (δ_{iso}), electric quadrupole splitting (Δ_{EQ}), and relative area of Fe ions. The Raman spectra were recorded on a HORIBA LabRAM HR Evolution with laser wavelength 532 nm. The EELS spectra were recorded on a probe aberration-corrected STEM (Cubed Titan G2 60-300, FEI, USA).

Electrochemical measurements

All the electrochemical measurements were carried out using a CHI 760 E Electrochemical Workstation (CHI Instruments, Shanghai Chenhua Instrument Corp., China) using a glass carbon electrode (geometric area = 0.071 cm^2) as the working

electrode, and Pt and Hg/HgO (1 M KOH) as auxiliary and reference electrodes in 1.0 M KOH solution. The potentials were referenced to a reversible hydrogen electrode (RHE) through the equation (E(RHE) = $E_{(Hg/HgO)}$ + 0.0951pH + 0.098). All electrochemical experiments were conducted at 20 ± 0.2 °C. The Ir/C (20%) catalysts were prepared according to a reported method.[25,31] The loading amount of the catalysts was 0.2 mg cm^{-2}. Electrochemical impedance spectroscopy (EIS) measurements were performed by applying an AC voltage with 5 mV amplitude in a frequency range from 100 000 to 0.01 Hz and recorded at 1.58 V *vs.* RHE. The electrical double layer capacitance (C_{dl}) and surface roughness factor (R_f) of the as-synthesized materials were measured from double-layer charging curves using cyclic voltammograms (CVs) in a small potential range of 1.17–1.27 V.

To investigate the reaction mechanism for the OER, rotating ring-disk electrode (RRDE) voltammograms were conducted on an RRDE configuration (RRDE-3A, Japan) consisting of a glassy carbon disk electrode and a Pt ring electrode. The loading amount was 0.2 mg cm^{-2}. A scan rate of 2 mV s^{-1} and a rotation rate of 1600 rpm were applied for RRDE tests. Specifically, to ensure that the oxidation current originates from oxygen evolution rather than other side reactions, and to calculate the faradaic efficiency of the system, the ring potential was held constant at 0.40 V *versus* RHE to reduce the O_2 formed from the catalyst on the disk electrode in N_2-saturated 1 M KOH solution. The faradaic efficiency (ε) was calculated as follows:

$$e = I_r/(I_d N)$$

where I_d denotes the disk current, I_r denotes the ring current, and N denotes the current collection efficiency of the RRDE. To properly calculate the faradaic efficiency of the system, the disk electrode was held at a relatively small constant current of 200 μA. This current is sufficiently large to ensure appreciable O_2 production and sufficiently small to minimize local saturation and bubble formation at the disk electrode.

The electron transfer number (n) during the ORR was calculated from the Koutecky–Levich (K–L) equations:[20]

$$\frac{1}{j} = \frac{1}{j_L} + \frac{1}{j_K} = \frac{1}{B\omega^{\frac{1}{2}}} + \frac{1}{j_K}$$

$$B = 0.2nFC_0D_0^{\frac{2}{3}}\nu^{\frac{-1}{6}}$$

where j, j_L, and j_K correspond to the measured, diffusion-limiting, and kinetic current densities, respectively; ω is the rotation rate (rpm), F is the Faraday constant (96 485C mol^{-1}), C_0 is the bulk concentration of oxygen (1.26×10^{-6} mol cm^{-3}), D_0 is the diffusion coefficient of oxygen (1.9×10^{-5} cm^2 s^{-1}), and n is the kinetic viscosity (0.01 cm^2 s^{-1}).

Al–air battery assembly

An aluminium sheet and $FeCoS_x$-PBA/carbon black loaded on carbon cloth (2 mg cm^{-2}) served as the anode and air cathode, respectively. All as-prepared electrodes were directly used as the air cathodes and aluminium plates were polished to be used as the anodes. The liquid Al–air battery was assembled in 2 M KOH with ZnO and Na_2SnO_3 as an additive was used as the electrolyte to slow down the corrosion of aluminium.[21] The alkaline gel electrolyte was prepared by dissolving KOH, PVA, ZnO and Na_2SnO_3 in deionized water at 95 °C under vigorous stirring until the solution became clear. Flexible aluminium–air batteries were assembled by separating the air cathode and Al anode with the alkaline gel polymer. Galvanostatic discharge and charge measurements were carried out with the LAND CT2001A multichannel battery testing system.

Computational method

In this work, simplified rotationally invariant DFT + U calculations[22] within the CASTEP code[23] were applied for all the calculations. The GGA and PBE exchange-correlation functionals were selected and the plane-wave cutoff energy was set to 750 eV.[24,25] Meanwhile, for all the geometric optimizations, the algorithm of Broyden–Fletcher–Goldfarb–Shanno (BFGS) was selected.[26] In addition, the ensemble DFT (EDFT) by Marzari *et al.*[27] was applied during the electronic-minimization process, which aims to improve the convergence quality of the transition metal in the $FeCoS_x$-PBA composite system.

By utilizing the OPIUM code in the Kleinman–Bylander projector form,[28] the norm-conserving pseudopotentials of Fe, Co, C, N, O, and H were generated with the incorporation of non-linear partial core correction[29] and a scalar relativistic averaging scheme.[30] The valence states of Fe, Co, C, N, O, and H were chosen as (3d, 4s, 4p), (3d, 4s, 4p), (2s, 2p), (2s, 2p), (2s, 2p) and (1s), respectively. The RRKJ method was applied for the optimization of the pseudopotentials.[31]

Two different models of $FeCoS_x$-PBA were constructed based on two different bonding situations at the interface: S bonding dominant and Fe–S bonding dominant. The vacuum space of $FeCoS_x$-PBA was set to 15 Å, which guarantees sufficient space for all the geometric optimizations. Considering the DFT computational cost, Monkhorst–Pack reciprocal space integration was performed using Gamma-center-off special k-points with a mesh of 2 × 2 × 2,[32] which was guided by the initial convergence test. The overall total convergence settings were set so that the total energy for each step was less than 5.0×10^{-7} eV per atom while the Hellmann–Feynman forces on the atom should not exceed 0.001 eV $Å^{-1}$.

Results and discussion

$FeCoS_x$-PBA hetero-nanoframes were synthesized by a sequential ultrasound-assisted ion-exchange method. The initial PBA nanocubes were ultrasonicated in dilute HCl solution containing Fe^{2+}, leading to the partial replacement of Co^{2+} with Fe^{2+} in the PBA surface and the formation of Fe/Co mixed Prussian blue analogue (MPBA) nanocubes, which provided a basis for the further synthesis of an $FeCoS_x$ structure. Further solvothermal treatment was performed to achieve S^{2-} ion exchange with $Fe(CN)_6^{3-}$.

The crystal structures of PBA, MPBA, and $FeCoS_x$-PBA (Fig. 1a) were studied by X-ray diffraction (XRD). The results of all three samples match well with the standard diffraction pattern representing a Prussian blue structure. Furthermore, after the introduction of S into MPBA, $FeCoS_x$-PBA also shows the same XRD pattern as MPBA, demonstrating that the major component of $FeCoS_x$-PBA is still MPBA. During the solvothermal reaction process, a low concentration of S^{2-} was released from thioacetamide (TAA). Then S^{2-} inactivated by ethanol favors the incomplete decomposition of MPBA, resulting in the partial retention of the Prussian blue structure.[17–19] It is worth noting that the (111) diffraction peaks are 17.80°, 17.57° and 17.43° in PBA, MPBA, and $FeCoS_x$-PBA, respectively (Fig. 1a). The continuous negative shift of the XRD diffraction peak reveals the expansion in lattice distance caused by the successful introduction of hetero cation (Fe^{2+}) and anion (S^{2-}).

The morphology was study by scanning electron microscopy (SEM) and transmission electron microscopy (TEM). The results show PBA exhibits a nanocube morphology with a diameter of about 250 nm (Fig. S1†). After Fe^{2+} ion exchange, the MPBA nanocubes had a nearly unchanged diameter and morphology (Fig. S2†). The Fe^{2+} ion exchange process was also studied by the same ultrasonic experiment without the addition of Fe^{2+}. As can be seen, the PBA nanocubes were corroded and broken into porous nanocubes (Fig. S3†). The above results indicate that Fe^{2+} has stronger bonding than Co^{2+} with $[Fe(CN)_6]^{3-}$ and can resist corrosion by HCl, which drives the Fe^{2+} ion-exchange process. After ion exchange with S^{2-}, the SEM image of $FeCoS_x$-PBA in Fig. 1b clearly shows a typical cubic shape with numerous small nanoparticles attached on the surface. The TEM image further confirms the hollow cube-like structure of $FeCoS_x$-PBA with an outer diameter of about 250 nm and

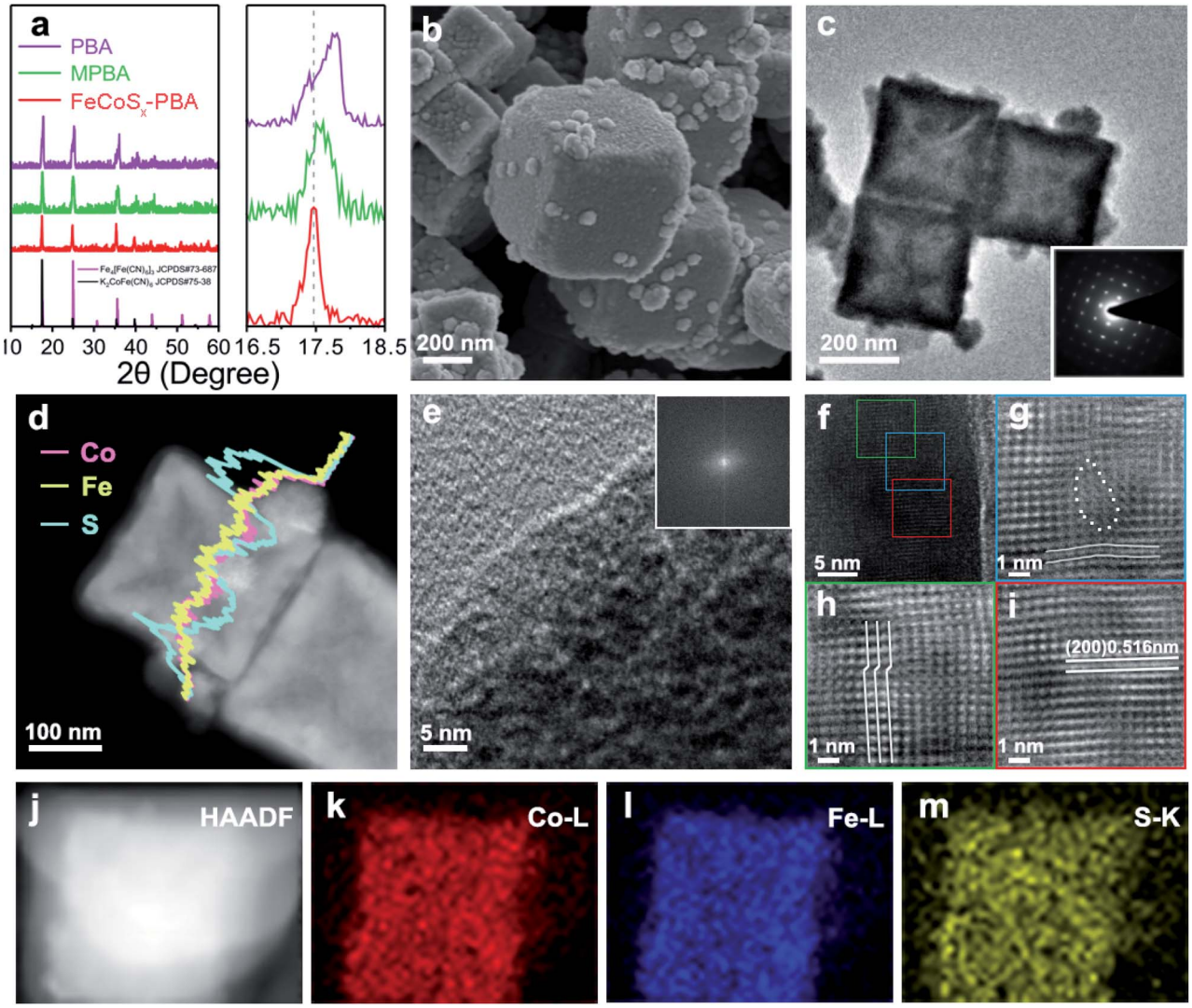

Fig. 1 (a) Powder XRD patterns of PBA, MPBA, and $FeCoS_x$-PBA (left). The corresponding XRD patterns range from 16° to 19° (right). (b) SEM image of $FeCoS_x$-PBA. (c) TEM image of $FeCoS_x$-PBA, and the corresponding SAED image (inset). (d) EDX line scan of a single $FeCoS_x$-PBA hetero-nanoframe. (e) HRTEM image of a nanoparticle in the surface of $FeCoS_x$-PBA, and the corresponding FFT image (inset). (f) HRTEM image of the skeleton part in FeCoSx-PBA. (g–i) Magnified HRTEM images extracted by inverse Fourier filtering of blue, red and green boxes in (f). EDX mapping of $FeCoS_x$-PBA in (j) HAADF-image, (k) Co L edge, (i) Fe L edge, (m) S K edge.

a skeleton thickness of 20–40 nm. The attached surface nanoparticles ranged from 30 nm to 50 nm. The Brunauer–Emmett–Teller (BET) results (Fig. S4 and Table S1†) also support the hollow structure of $FeCoS_x$-PBA, which has a significantly increased BET surface area from ~8.9 $m^2 g^{-1}$ to ~28.9 $m^2 g^{-1}$.

To determine the structural changes caused by the introduction of S, TEM was further performed on $FeCoS_x$-PBA. The remarkable single crystal structure with a cubic system was also confirmed by the selected area electron diffraction (SAED) images in the *inset* of Fig. 1c. Combined with the XRD results, this indicated that the hollow cube is mainly an MPBA structure. The energy-dispersive X-ray spectroscopy (EDX) element line scan profile demonstrates the uniform distribution of Fe and Co of $FeCoS_x$-PBA (Fig. 1d). The S content is significantly higher in the surface nanoparticles than in the skeleton part. This suggests that the surface nanoparticles may be a $FeCoS_x$ sulfide. High-resolution transmission electron microscopy (HRTEM) was used to study the lattice structure of $FeCoS_x$-PBA further. As shown in Fig. 1e, no lattice fringe can be observed for the surface particle. Its corresponding fast Fourier transform (FFT) image (insert of Fig. 1e) also shows no diffraction spots, revealing the amorphous feature of $FeCoS_x$. The amorphous structure was also evidenced by a contrast experiment, where MPBA reacted with Na_2S instead of TAA under the same experimental conditions to fully convert Prussian blue to sulfide. The as-obtained materials show no XRD peak (Fig. S5†), revealing the amorphous structure.

The skeleton part of $FeCoS_x$-PBA displayed legible lattice fringes, which can be ascribed to the (200) planes of K_2-$CoFe(CN)_6$ and $Fe_4[Fe(CN)_6]_3$ in Fig. 1f and S6.† Three parts marked in green, blue, and red frames were chosen to remove background noise by the inverse Fourier filtering method and are shown in Fig. 1g–i. Fig. 1g shows significant lattice distortions marked by lines and a large area of vacancy defects marked by dots. Fig. 1h displays characteristic lattice dislocations of ~0.23 nm, in which the periodic arrangement of atoms mismatches and slides. Fig. 1i illustrates a representative HRTEM image, in which the marked lattice spacing value is 0.516 nm that is assigned to the (200) plane of the Prussian blue structure. Compared to PBA and MPBA with lattice distances of 0.504 nm and 0.506 nm, respectively, $FeCoS_x$-PBA shows a small lattice expansion of 0.01 nm, which may be attributed to the flexible and framework-like lattice structure of ferricyanide. This S^{2-} doping and the resulting abundant lattice imperfections were proved to exist in $FeCoS_x$-PBA and could be expected to promote the electrocatalytic performance.[33–35] The element mappings in Fig. 1j–m also demonstrate the distributions of Fe, Co, and S in $FeCoS_x$-PBA.

The above results indicated that the S atom has two primary forms in $FeCoS_x$-PBA. One is S^{2-} in $FeCoS_x$, and the other is doped S in Prussian blue (Fig. 2a). X-ray photoelectron spectroscopy (XPS) was performed to provide in-depth evidence and trace the differences in electronic structure among PBA, MPBA, and $FeCoS_x$-PBA (Fig. 2b–d, S7 and S8). Along with the introduction of S, the Co 2p spectrum of $FeCoS_x$-PBA in Fig. 2b was deconvoluted into two pairs of peaks at binding energies of 778.3 eV, 781.1 eV, 793.3 eV, and 797.3 eV, which were attributed to Co–S and Co–N species, respectively.[36,37] The Fe 2p spectrum of $FeCoS_x$-PBA (Fig. 2c) shows a similar structure to Co. The peaks at 708.1 eV and 720.7 eV belong to Fe–C species, while the peaks at 708.5 eV and 721.8 eV belong to Fe–S species.[38,39] Moreover, the S 2p spectrum of $FeCoS_x$-PBA (Fig. 2d) can be identified as two pairs of peaks with binding energies of 161.8 eV, 163.0 eV, 163.9 eV, and 165.0 eV. The former two peaks can be assigned to Fe/Co–S groups, and the latter two belong to C–S groups.[33–35] From these results, it can be found that doped S atom in $FeCoS_x$-PBA bonds with the C atom of the cyanide ligands to form a C–S structure. This suggestion was further confirmed by C 1s XPS spectra, where a new peak centered at 285.6 eV is observed for $FeCoS_x$-PBA and can be assigned to the C–S structure (Fig. S8†).[40] Other peaks at 284.6 eV, 286.7 eV, and 288.7 eV are attributed to C=C–C, C–O/C–N, and C=O, respectively.[41,42] In addition, N coordination was verified by the N 1s spectra. Three types of nitrogen peaks of $FeCoS_x$-PBA were fitted at 397.1 eV, 398.3 eV, and 401.8 eV, which are attributed to Fe/Co–N, C–N, and N–H species.[43,44] Furthermore, a significant peak shift was observed after the introduction of S. The original Co–N and Fe–C peaks appear to have negative shifts of 0.8 eV and 0.5 eV, indicating the increased electron density of the Co and Fe atoms. The electrical effect of the S atoms was further spread to the adjacent N and C atoms. The negative shift and positive peak shift of N and C, respectively, revealed that the electron density in the C and N atoms decreased and increased separately. Besides, a significantly enhanced N–H peak at 401.8 eV observed in $FeCoS_x$-PBA also demonstrates that N atoms become more electronegative and more accessible for combining with hydrogen molecules in the atmosphere to form N–H-like species.[43,44] The above results further support the two primary forms of S in $FeCoS_x$-PBA.

To provide further detail about the local electronic structure, electron energy loss spectroscopy (EELS) was performed. Especially for $FeCoS_x$-PBA, the PBA frame region and amorphous $FeCoS_x$ particles region were studied separately (Fig. S9†). First, the Fe $L_{2,3}$ white lines (Fig. 2e) show a 0.5 eV negative shift from PBA to MPBA, which indicates a slight decrease in the valence state of Fe. This is consistent with the introduction of Fe^{2+} into MPBA. Thus, the Co and Fe $L_{2,3}$ spectra of the PBA frame region in $FeCoS_x$-PBA indicate a small change compared with MPBA. This shows that the doped S influences the valence state of Co and Fe in the PBA framework. But the Co and Fe $L_{2,3}$ spectra of the amorphous $FeCoS_x$ region in $FeCoS_x$-PBA exhibit a 1 eV positive shift compared with the PBA frame region. This represents a significant structural difference between the PBA structure and the sulfide structure.[45] The intensity of the S $L_{2,3}$ white lines (Fig. 2f) in the PBA frame region is lower than in the amorphous $FeCoS_x$ region and has a 0.5 eV difference. This also shows the different forms of S in $FeCoS_x$-PBA.[46,47] Mössbauer spectroscopy was further employed to analyze different Fe species. The Mössbauer spectrum of $FeCoS_x$-PBA (Fig. 2g) was fitted with a single and a doublet assigned to Fe(II)–C/N and Fe(II)–S species, respectively. The Mössbauer spectra of PBA and MPBA (Fig. S10 and S11†) were fitted with a single and a doublet but assigned to low-spin Fe(II) and high-spin Fe(III) species, respectively.[48,49] After introducing Fe^{2+}, the region ratio of

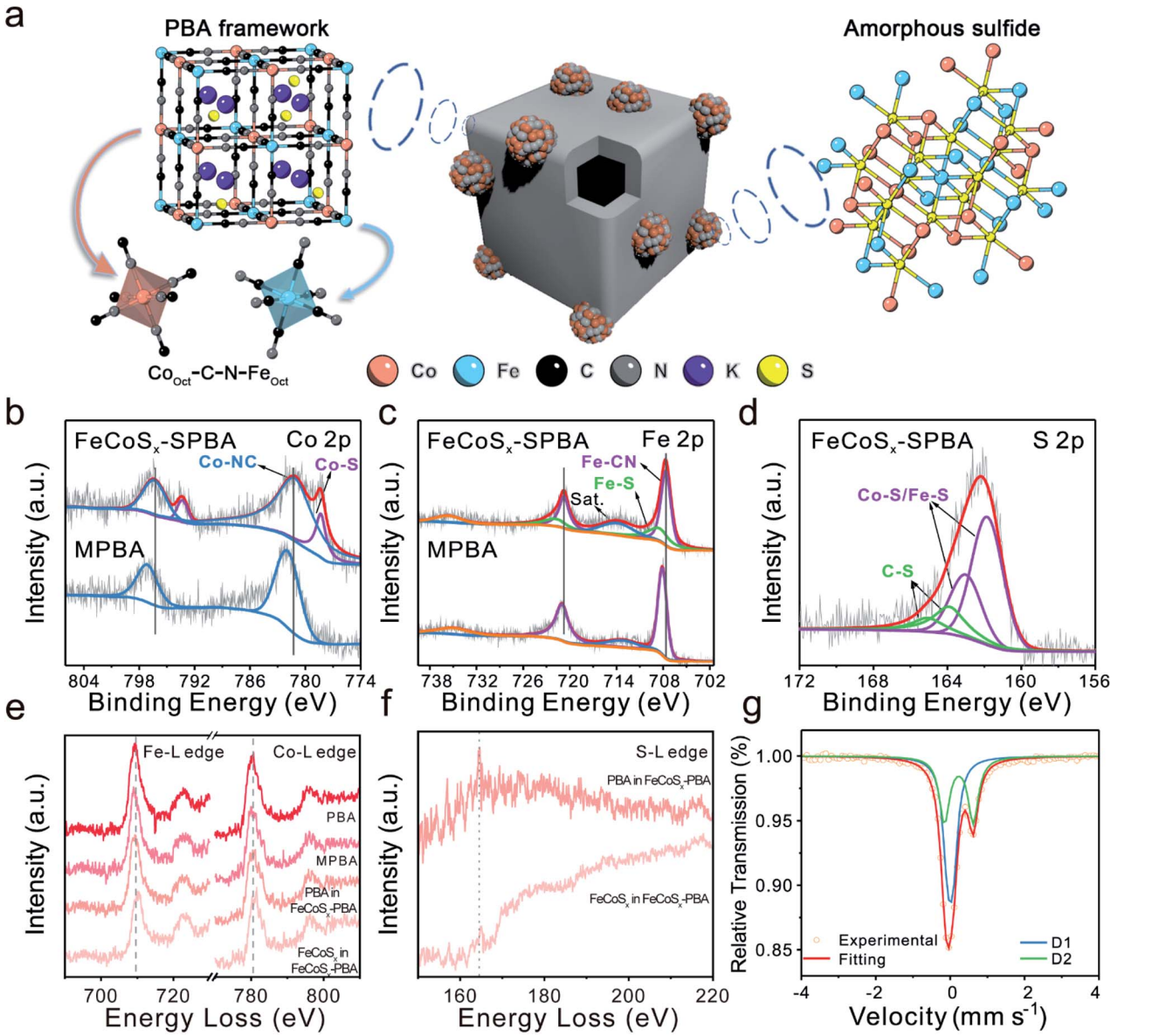

Fig. 2 (a) Schematic diagrams of $FeCoS_x$-PBA. (b) Co 2p and (c) Fe 2p XPS spectra of $FeCoS_x$-PBA and MPBA. (d) S 2p XPS spectra of $FeCoS_x$-PBA. (e) Co $L_{2,3}$ and Fe $L_{2,3}$ edge EELS spectra of PBA, MPBA, and $FeCoS_x$-PBA. (f) S $L_{2,3}$ edge EELS spectra of $FeCoS_x$-PBA. (g) Mössbauer spectrum pattern of $FeCoS_x$-PBA.

single : doublet in MPBA increased, showing an increased Fe^{2+}/Fe^{3+} ratio from 1.46 to 2.91. The corresponding fitting parameters and the relative peak area for the catalysts are summarized in Table S2.†

Then we introduced DFT calculations to unravel the significant improvements in OER performance in the $FeCoS_x$-PBA hybrid systems. Although the cage structure of PBA endows them with a stable structure with a high surface area, the low electronic conductivity still leads to limited application in the electrocatalyst. With the introduction of $FeCoS_x$ on the surface with different bonding situations, the electroactivity of PBA has been activated on the surface-defective $FeCoS_x$ layer with large exposure of active sites. The bonding and anti-bonding orbitals near the Fermi level (E_F) are mostly dominated by the surface $FeCoS_x$ layers. Meanwhile, the remarkable stability of the PBA structural frame determines the long-term durability of the composite electrocatalyst (Fig. 3a). Thus, the projected partial density of states (PDOS) of S, Fe, Co, and –CN functional groups in $FeCoS_x$-PBA are illustrated. Except for the surface, S sites demonstrate broad S-3p orbitals, covering from E_V −8.0 eV to E_V +3.5 eV (E_V = 0 eV). However, the surface-unsaturated S shows a strong delocalization feature with the dominant peak at E_V −4.7 eV, which effectively suppresses the overbinding effect of –OH in the alkaline environment (Fig. 3b). From the bulk to the surface, the e_g of Fe-3d orbitals significantly shifts from E_V +4.5 eV to E_V +0.6 eV. The downshifting of the d-band center of surface Fe is also noted, which boosts both electron transfer and binding with the OH group. Meanwhile, the surface Fe

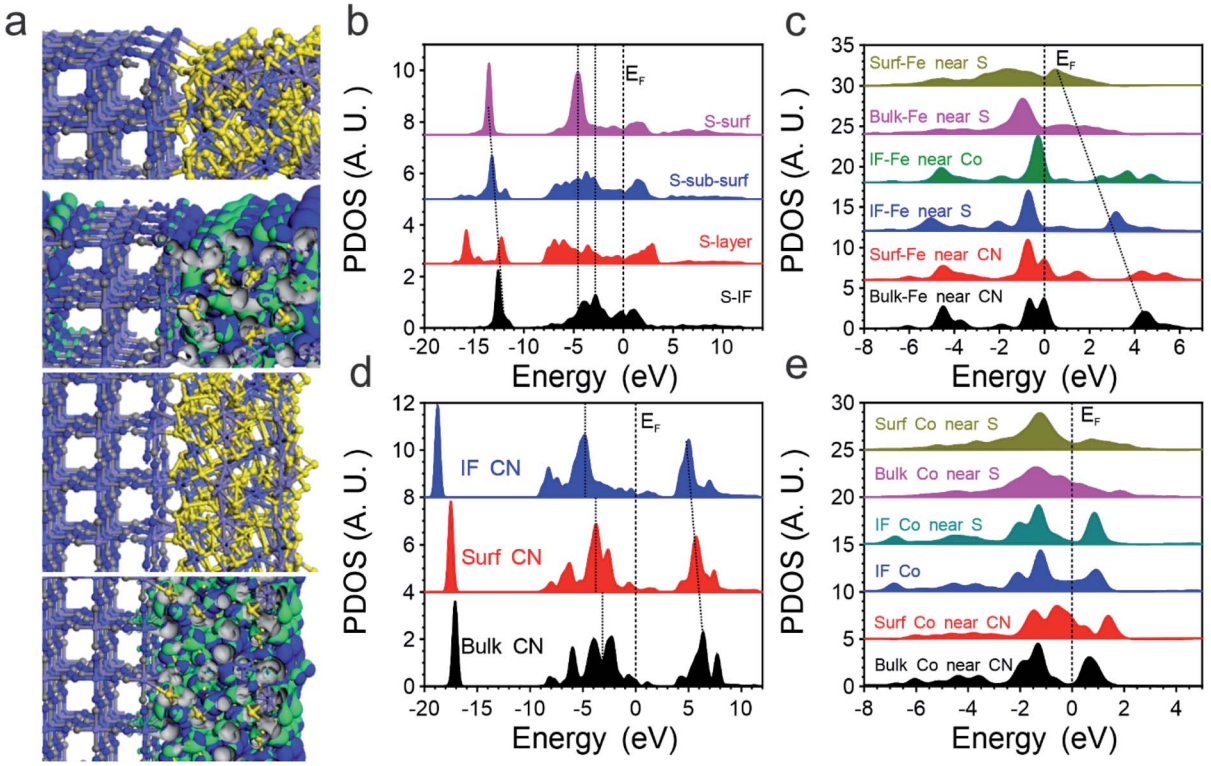

Fig. 3 The electronic structures of $FeCoS_x$-PBA. (a) Structural configurations and real spatial 3D orbital contour plots of two different $FeCoS_x$-PBA systems. (b) Site-dependent PDOSs of S in $FeCoS_x$-PBA. (c) Site-dependent PDOSs of Fe in $FeCoS_x$-PBA. (d) Site-dependent PDOSs of Co in $FeCoS_x$-PBA. (e) Site-dependent PDOSs of –CN in $FeCoS_x$-PBA.

indicates the evident crossing of E_F, supporting the reduction of valence state with improved electronic conductivity. This significantly compensates for the poor electron transfer capability in pristine PBA (Fig. 3c). For Co-3d orbitals, we notice the evident splitting of t_2g and e_g in PBA-Co and the interfacial Co. Only Co sites in the surface $FeCoS_x$ layer demonstrate the increased electron density of 3d orbitals near E_F to further enhance the electron transfer (Fig. 3d), which is consistent with the XPS results. In addition, the CN groups in PBA were also investigated regarding their electronic structures. From the bulk PBA to the interfacial region binding with $FeCoS_x$, the s,p orbitals of –CN groups demonstrate a gradual downshift away from the E_F, becoming more electronegative, which confirms the experimental characterizations. This also means that the introduction of the surface $FeCoS_x$ layers not only leads to modified –CN functional groups with improved stability but also the overbinding poisoning of OH groups during the OER (Fig. 3e).

The OER activity was studied in an alkaline medium (1.0 M KOH) through linear sweep voltammetry (LSV) (Fig. 4a) for the as-prepared three catalysts and benchmark Ir/C (20%) which were prepared on glassy carbon electrodes. After modifying the outermost surface of PBA by Fe^{2+}, the as-obtained MPBA has an obviously enhanced catalytic performance with 75 mV increased overpotential at 10 mA cm^{-2} compared with PBA. Furthermore, $FeCoS_x$-PBA with further optimization of the electronic structure shows the best OER activity among all these samples, including commercial Ir/C. Its overpotential at a current density of 10 mA cm^{-2} is approximately 266 mV, much lower than those of Ir/C (320 mV), PBA (409 mV), or MPBA (334 mV). The Tafel plot is an inherent parameter for evaluating OER catalytic kinetics. The lowest Tafel slope of 33 mV dec^{-1} (Fig. 4b) for $FeCoS_x$-PBA suggested the fastest OER dynamics. Long-term stability is another crucial criterion in evaluating the catalytic property. Hence, the chronoamperometric response was carried out at a constant current density of ~8 mA cm^{-2}. After 15 hours of testing, $FeCoS_x$-PBA still retains 91.4% current, indicating its superior durability (Fig. S12†). To eliminate the influence of corrosion current, a faradaic efficiency study was performed on a rotating ring-disk electrode (RRDE) in N_2-saturated 1 M KOH (Fig. S13†). With the disk current held constant at 200 μA, a ring current of ~38.3 μA was detected, which proved that the observed OER current catalyzed by $FeCoS_x$-PBA could be mainly attributed to the OER with a high faradaic efficiency of 95.7%.

To gain deeper insight into the OER activity of $FeCoS_x$-PBA, the electrochemical impedance spectra (EIS) were taken and an electrochemical double-layer capacitance (C_{dl}) test was performed. The C_{dl} of $FeCoS_x$-PBA, MPBA, and PBA (Fig. S14†) were confirmed to be 24.3 mF cm^{-2}, 11.8 mF cm^{-2}, and 8.2 mF cm^{-2}, respectively. Combined with BET results (Fig. S4†), $FeCoS_x$-PBA performed with better exposure and enhanced electroactive sites. In order to clarify the intrinsic activity differences of the above materials, the catalytic current was normalized to electrode geometric area, BET surface area, and ECSA, respectively.

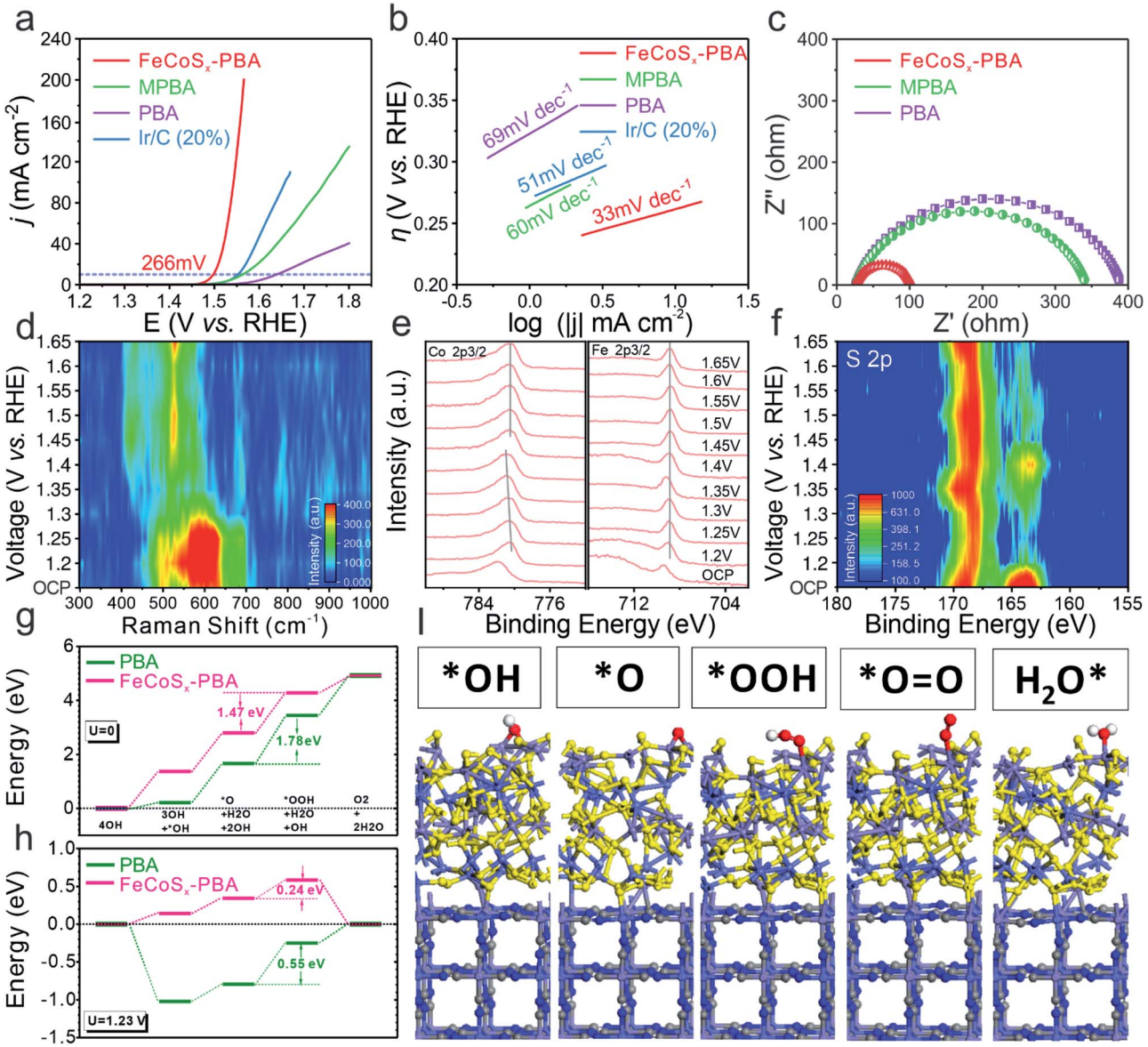

Fig. 4 (a) Polarization curves and (b) Tafel plots of PBA, MPBA, $FeCoS_x$-PBA and commercial Ir/C (20%) in an O_2-saturated 1 M KOH solution (scan rate 2 mV s^{-1}). (c) EIS spectra of PBA, MPBA and $FeCoS_x$-PBA. (d) *In situ* Raman spectra of $FeCoS_x$-PBA during the OER. (e) *Quasi-in situ* Co 2p3/2 and Fe 2p3/2 XPS spectra of $FeCoS_x$-PBA during the OER. (f) *Quasi-in situ* S 2p XPS spectra of $FeCoS_x$-PBA during the OER. (g) The OER reaction pathways of $FeCoS_x$-PBA and PBA in the alkaline environment at the equilibrium state (U = 0 V). (h) The OER reaction pathways of $FeCoS_x$-PBA and PBA in the alkaline environment with an applied potential of 1.23 V. (i) The structural configurations of adsorption of key intermediates on $FeCoS_x$-PBA.

As shown in Fig. S15,† after eliminating the effect of surface area, $FeCoS_x$-PBA still performs with the best OER activity. This demonstrates that the superior OER activity of $FeCoS_x$-PBA is due to the co-optimization of electronic structure and morphology. In the Nyquist plots (Fig. 4c), PBA displays the largest charge transfer resistance (R_{ct}), and MPBA shows a 12% reduced R_{ct} value. Undoubtedly, $FeCoS_x$-PBA has the lowest R_{ct} of all three catalysts. It is only approximately a quarter of PBA, which suggests the faster electron transfer ability during the OER in $FeCoS_x$-PBA. This result further proved that the electron structure was modified from PBA to $FeCoS_x$-PBA along with the decreasing R_{ct}. The important role of PBA frameworks in the OER was also unraveled by a contrast experiment. As shown in Fig. S16,† amorphous $FeCoS_x$ shows poor OER activities compared to $FeCoS_x$-PBA. In addition, the stability test result of amorphous $FeCoS_x$ without a PBA framework is shown in Fig. S16.† This clearly indicates poor stability. The above results proved that an $FeCoS_x$ layer combined with a PBA structural frame determines the long-term durability of the composite electrocatalyst.

OER dynamic study is another vital tool for understanding the OER process and mechanism. *In situ* Raman and *quasi-in situ* XPS spectra were performed on $FeCoS_x$-PBA during the OER catalysis process. The *in situ* Raman spectrum (Fig. 4d and

S17†) shows the reconstruction of a catalyst at 1.35 V (*vs.* RHE) and the formation of CoFe oxy-hydroxides. The low reconstruction voltage is favorable for catalyzing the OER and could be caused by the large amount of defects in the amorphous structure. Further *quasi-in situ* XPS results unravel the electronic structure evolution of different elements at different applied OER voltages. As shown in Fig. 4e, with increased voltage, the valence state of Co also grows and becomes stable at a high value. But Fe offers a very steady valence state during the OER process. These results show that the Co sites facilitate site-to-site electron transfer and stabilize the Fe sites. Moreover, the S 2p *quasi-in situ* XPS result (Fig. 4f and S18†) shows the existence of residual sulfur in the catalysts during the OER. The increased adsorbed SO_4^{2-} peak also indicated that lattice S in $FeCoS_x$-PBA is partially oxidized to SO_4^{2-} during the OER. The SO_4^{2-} would be adsorbed on the catalyst surface and promote the OER process.[50–53]

Then we further unravel the improved electroactivity of the $FeCoS_x$-PBA hybrid system based on the energetic reaction pathway. In the equilibrium state, the OER reaction pathway shows a continuous trend for both PBA and $FeCoS_x$-PBA composite systems. The reaction [*O + H_2O + 2OH] → [*OOH + H_2O + OH] is the rate-determining step for the OER due to its having the largest energy barrier. For pure PBA, the energy barrier is 1.78 eV, which is much larger than the 1.47 eV of the $FeCoS_x$-PBA composite system, confirming the enhanced electroactivity for the OER (Fig. 4g). With an applied standard potential of 1.23 V, the evident reaction trend is displayed. For pristine PBA, the initial OH adsorption of the alkaline OER is very strong, which leads to a nearly 1 eV energy drop. However, such a strong overbinding effect of OH also hinders the subsequent reactions, resulting in a 0.55 eV overpotential for the OER. In comparison, although the slightly weaker adsorption of OH on the $FeCoS_x$-PBA composite shows the initial uphill trend for the OER, the overall overpotential has been greatly lowered to 0.24 eV, which is highly consistent with the electrochemical performances (Fig. 4h). The stable adsorption of key intermediates shows that the O-related species prefer the Fe sites on the surface with mild adsorption strength to maintain efficient intermediate transformation. Meanwhile, the Co sites facilitate the site-to-site electron transfer from the surface, and S sites balance the optimal binding strength with OH groups within the alkaline environment. The stable structure of PBA after adsorption supports the long-term durability performances in the experiments (Fig. 4i). The above results are also consistent with the *quasi-in situ* XPS results (Fig. 4e, f and S18†).

To evaluate the Al–air battery performance of $FeCoS_x$-PBA, the oxygen reduction reaction (ORR) performance was evaluated first in Fig. S19.† $FeCoS_x$-PBA indicates an optimized half-wave potential and diffusion-limited current density. The electron transfer number of $FeCoS_x$-PBA is 3.3. Then a liquid Al–air battery was assembled with 2 M KOH. Polarization curves (Fig. 5b) indicated that the maximum power density of $FeCoS_x$-PBA is 58.3 mW cm^{-2}. The capacity property was studied by galvanostatic discharge curves. As shown in Fig. 5c, $FeCoS_x$-PBA generates a large specific capacity of 1259 mA h g^{-1} at a current density 1 mA cm^{-2}, and the energy density was calculated as 1483 W h kg^{-1}. When the current density increased to 5 mA cm^{-2}, the specific capacity and energy density also decreased to 1091 mA h g^{-1} and 1199 W h kg^{-1}, respectively. Furthermore, at a large discharge current density of 10 mA cm^{-2}, this Al–air battery still retains 1002 mA h g^{-1} capacity and 970 W h kg^{-1} energy density. These battery parameters of $FeCoS_x$-PBA materials are better than those of other materials in the literature to the best of our knowledge and indicate their great potential to serve as efficient air cathodes for clean energy storage and conversion applications. Due to the extremely high reduction potential of Al in aqueous solution, Al cannot be electrodeposited in aqueous electrolytes. Thus, the Al–air battery was not rechargeable. Hence, to assess the long-term stability of the $FeCoS_x$-PBA cathode, a mechanical recharge through replacing the Al sheet in the battery was performed. 10 hours was chosen as the period, and in all 5 periods, the Al–air battery retains a nearly unchanged discharge voltage, as shown in Fig. 5d. This result demonstrated that the $FeCoS_x$-PBA cathode exhibits superior long-term stability. Further, a blue-light-emitting diode was successfully lit by two series-connected Al–air batteries (Fig. S20†). Also, the Ragone diagram plotting the energy and power densities of the fabricated device compared to those reported Al–air batteries are depicted in Fig. 5e and Table S4.†

Driven by the increasing demand for flexible and wearable electronic devices, solid Al–air batteries were further fabricated with $FeCoS_x$-PBA/carbon black material supported on carbon cloth as the air cathode, aluminium sheet as the metal anode, and alkaline polyvinyl alcohol/polyethylene glycol as the gel electrolyte (Fig. 5a). The fabricated battery exhibited outstanding bendability and stretchability. Fig. 5f shows a single battery displaying an open circuit voltage of 1.44 V, and two batteries in series exhibiting an open-circuit voltage of 2.94 V. The hydrogel used in the battery endows it with excellent flexibility (Fig. S21†). At a discharge current of 1 mA, this solid Al-battery was bent to 60, 120, and 180° and its discharge performance was almost constant because its discharge voltage only slightly decreased (Fig. 5g). When the battery was stretched by 10%, 20%, and 30%, it did not break upon elongation. After stretching 10% to 30%, the battery had a gradually decreasing discharge voltage at 1 mA cm^{-2}, but the amplitude of the voltage decrease is small. Even up to 30%, the battery output voltage was also maintained above 1 V during stretching (Fig. 5h). It is easy to understand that stretched batteries will increase charge and mass transfer distance and hinder battery performance. From the above results, this solid flexible Al–air battery displays remarkable bendability and stretchability. The actual application shows that a device with four batteries connected in series can charge a smartphone from 20% electricity to full charge (Fig. 5i) under various bending conditions from 0° to 360°.

Conclusions

In summary, we have successfully developed a unique hollow $FeCoS_x$-PBA hetero-nanoframe catalyst *via* an ultrasound-assisted ion-exchange procedure. The introduction of hetero

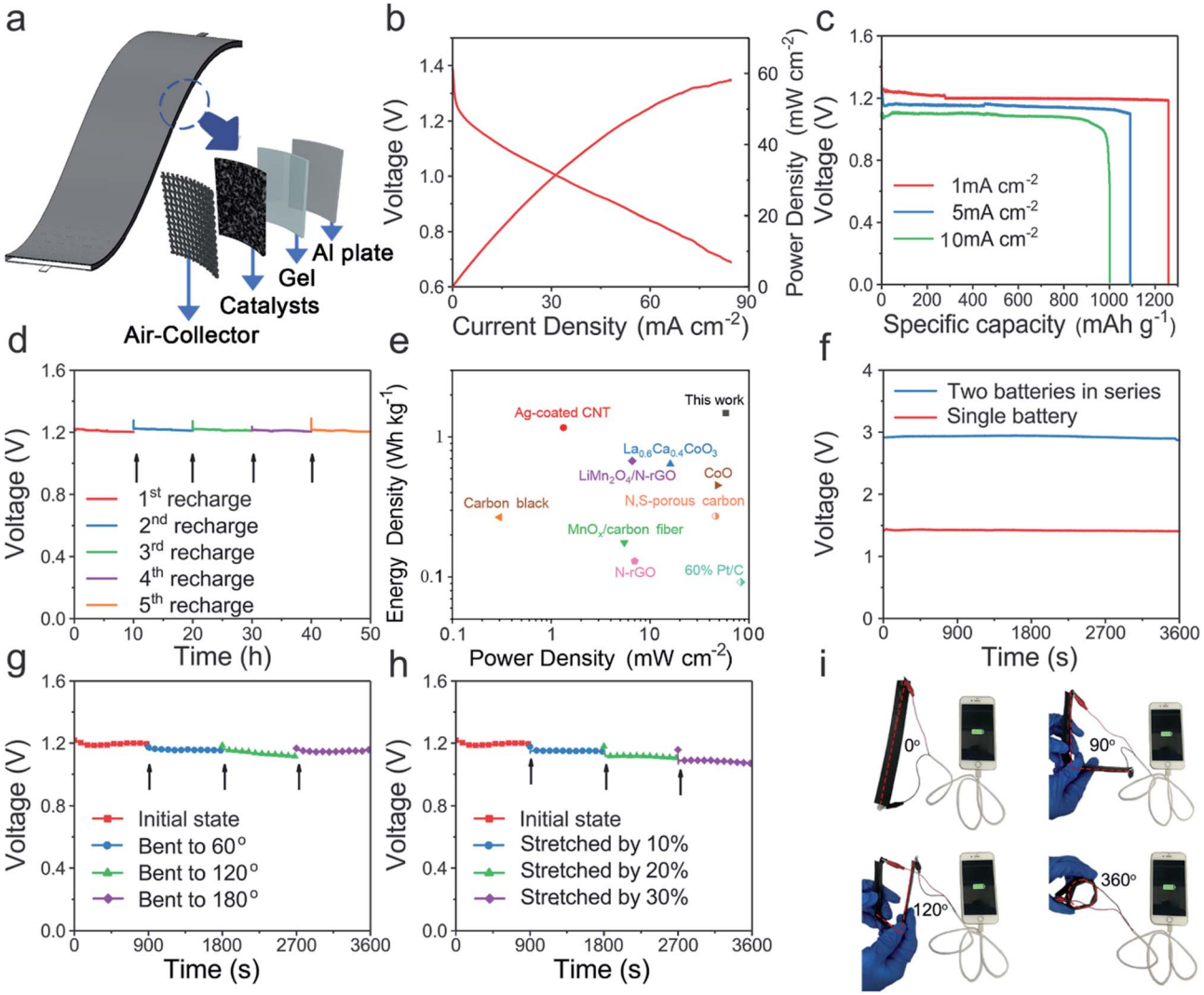

Fig. 5 (a) Schematic diagram of flexible Al–air batteries. (b) Polarization and power density curves of the Al–air batteries. (c) Galvanostatic discharge curves at 1 mA cm^{-2}, 5 mA cm^{-2}, 10 mA cm^{-2} of Al–air batteries. (d) Discharge curves at 1 mA cm^{-2} and recharged by replacing Al foil. (e) Ragone plots of the Al–air batteries. The values reported for other energy storage devices are added for comparison. (f) Open circuit voltage–time curves of one and two solid Al–air batteries. (g–h) Discharge curves of wearable Al–air batteries at different bending angles or stretching ratios at a discharge current of 1 mA. (i) Photographs of four batteries in series charging a smartphone with bending angles 0°, 90°, 120°, and 360°.

Fe and S atoms modifies the intrinsic electronic structure of the Co site. DFT calculations further confirm that the surface $FeCoS_x$ layer significantly enhances the electron transfer capability of PBA to achieve an efficient OER process. The suppression of OH overbinding also guarantees the efficient transformation of the intermediate. Meanwhile, the stable structure of PBA protected by the surface $FeCoS_x$ layer is the critical factor for the long-term durability of the electrocatalyst. The above morphological and structural advantages provide more exposed active sites and an optimized intrinsic electronic structure, which dramatically enhances the catalytic activity. Moreover, the $FeCoS_x$-PBA cathode can drive a solid Al–air battery with remarkable bendability, stretchability, and a high specific capacity of 1259 mA h g^{-1} at 1 mA cm^{-2}. This work may expand the toolbox of strategies to design and synthesize high-performance energy-related catalysts in terms of morphology and structure through electronic engineering.

Conflicts of interest

There are no conflicts to declare.

Acknowledgements

We acknowledge support from the National Natural Science Foundation of China (No. 21931001 and 21922105), the Special Fund Project of Guiding Scientific and Technological Innovation Development of Gansu Province (2019ZX-04) and the 111 Project (B20027). We also acknowledge support by the Fundamental Research Funds for the Central Universities (lzujbky-

2021-pd04, lzujbky-2021-it12 and lzujbky-2021-37). B. H. acknowledges the support of the Natural Science Foundation of China (NSFC) (No. 21771156) and the Early Career Scheme (ECS) fund (Grant PolyU 253026/16P) from the Research Grant Council (RGC) in Hong Kong. J. Y. acknowledges the support of the China Postdoctoral Science Foundation (2021M691375) and the China National Postdoctoral Program for Innovative Talents (BX20200157).

References

1 C. Steven and A. Majumdar, *Nature*, 2012, **488**, 294.
2 J. Suntivich, H. A. Gasteiger, N. Yabuuchi, H. Nakanishi, J. B. Goodenough and S. H. Yang, *Nat. Chem.*, 2011, **3**, 546.
3 A. Kudo and Y. Miseki, *Chem. Soc. Rev.*, 2009, **38**, 253.
4 M. W. Kanan and D. G. Nocera, *Science*, 2008, **321**, 1072.
5 L. An, Z. Zhang, J. Feng, F. Lv, Y. Li, R. Wang, M. Lu, R. B. Gupta, P. Xi and S. Zhang, *J. Am. Chem. Soc.*, 2018, **140**, 17624.
6 Y. Lee, J. Suntivich, K. J. May, E. E. Perry and S. H. Yang, *J. Phys. Chem.*, 2012, **3**, 399.
7 J. Suntivich, K. J. May, H. A. Gasteiger, J. B. Goodenough and S. H. Yang, *Science*, 2011, **334**, 1383.
8 F. Cheng and J. Chen, *Chem. Soc. Rev.*, 2012, **41**, 2172.
9 H. Zhang, J. Wang, Q. Cheng, P. Saha and H. Jiang, *Green Energy Environ.*, 2020, **5**, 492.
10 X. Y. Yu, Y. Feng, Y. Jeon, B. Guan, X. W. D. Lou and U. Paik, *Adv. Mater.*, 2016, **28**, 9006.
11 J. Nai, Y. Lu, L. Yu, X. Wang and X. W. D. Lou, *Adv. Mater.*, 2017, **29**, 1703870.
12 R. Wang, Y. Wei, L. An, R. Yang, L. Guo, Z. Weng, P. Da, W. Chen, J. Jin, J. Li and P. Xi, *Chin. J. Chem.*, 2020, **38**, 772.
13 S. Liu, M. Wang, X. Sun, N. Xu, J. Liu, Y. Wang, T. Qian and C. Yan, *Adv. Mater.*, 2018, **30**, 12876.
14 V. R. Stamenkovic, B. Fowler, B. Simon Mun, G. Wang, P. N. Ross, C. A. Lucas and N. M. Marković, *Science*, 2007, **315**, 493.
15 B. Hammer and J. K. Nørskov, *Surf. Sci.*, 1995, **343**, 211.
16 F. Cheng, J. Shen, B. Peng, Y. Pan, Z. Tao and J. Chen, *Nat. Chem.*, 2011, **3**, 79.
17 L. Han, X. Y. Yu and X. W. Lou, *Adv. Mater.*, 2016, **28**, 4601.
18 X. Y. Yu, L. Yu, H. B. Wu and X. W. Lou, *Adv. Mater.*, 2015, **127**, 5421.
19 G. Yilmaz, K. M. Yam, C. Zhang, H. J. Fan and G. W. Ho, *Adv. Mater.*, 2017, **29**, 1606814.
20 X. Zhong, M. Oubla, X. Wang, Y. Huang, H. Zeng, S. Wang, K. Liu, J. Zhou, L. He, H. Zhong, N. Alonso-Vante, C.-W. Wang, W.-B. Wu, H.-J. Lin, C.-T. Chen, Z. Hu, Y. Huang and J. Ma, *Nat. Commun.*, 2021, **12**, 3136.
21 Y. Xu, Y. Zhao, J. Ren, Y. Zhang and H. Peng, *Angew. Chem., Int. Ed.*, 2016, **128**, 8111.
22 I. A. Vladimir, F. Aryasetiawan and A. I. Lichtenstein, *J. Phys.: Condens. Matter*, 1997, **9**, 767.
23 S. J. Clark, M. D. Segall, C. J. Pickard, P. J. Hasnip, M. I. J. Probert, K. Refson and M. C. Payne, *Z. Kristallogr.*, 2005, **220**, 567.
24 J. P. Perdew, K. Burke and M. Ernzerhof, *Phys. Rev. Lett.*, 1996, **77**, 3865.
25 J. P. Perdew, M. Ernzerhof and K. Burke, *J. Chem. Phys.*, 1996, **105**, 9982.
26 J. D. Head and M. C. Zerner, *Chem. Phys. Lett.*, 1985, **122**, 264.
27 N. Marzari, D. Vanderbilt and M. C. Payne, *Phys. Rev. Lett.*, 1997, **79**, 1337.
28 L. Kleinman and D. M. Bylander, *Phys. Rev. Lett.*, 1982, **48**, 1425.
29 S. G. Louie, S. Froyen and M. L. Cohen, *Phys. Rev. B*, 1982, **26**, 1738.
30 I. Grinberg, N. J. Ramer and A. M. Rappe, *Phys. Rev. B*, 2000, **62**, 2311.
31 A. M. Rappe, K. M. Rabe, E. Kaxiras and J. D. Joannopoulos, *Phys. Rev. B*, 1990, **41**, 1227.
32 M. I. J. Probert and M. C. Payne, *Phys. Rev. B*, 2003, **67**, 075204.
33 Y. Ito, W. Cong, T. Fujita, Z. Tang and M. Chen, *Angew. Chem., Int. Ed.*, 2015, **54**, 2131.
34 Y. Dou, T. Liao, Z. Ma, D. Tian, Q. Liu, F. Xiao, Z. Sun, J. Ho Kim and S. Xue Dou, *Nano Energy*, 2016, **30**, 267.
35 Y. Liu, H. Cheng, M. Lyu, S. Fan, Q. Liu, W. Zhang, Y. Zhi, C. Wang, C. Xiao, S. Wei, B. Ye and Y. Xie, *J. Am. Chem. Soc.*, 2014, **136**, 15670.
36 Z. Chen, Y. Song, J. Cai, X. Zheng, D. Han, Y. Wu, Y. Zang, S. Niu, Y. Liu, J. Zhu, X. Liu and G. Wang, *Angew. Chem., Int. Ed.*, 2018, **57**, 5076.
37 F. Cao, M. Zhao, Y. Yu, B. Chen, Y. Huang, J. Yang, X. Cao, Q. Lu, X. Zhang, Z. Zhang, C. Tan and H. Zhang, *J. Am. Chem. Soc.*, 2016, **138**, 6924.
38 Y. Chen, R. Gokhale, A. Serov, K. Artyushkova and P. Atanassov, *Nano Energy*, 2017, **38**, 201.
39 Y. Li, Y. Wang, B. Pattengale, J. Yin, L. An, F. Cheng, Y. Li, J. Huang and P. Xi, *Nanoscale*, 2017, **9**, 9230.
40 D. R. Mullins and P. F. Lyman, *J. Phys. Chem.*, 1993, **97**, 9226.
41 J. Yin, Q. Fan, Y. Li, F. Cheng, P. Zhou, P. Xi and S. Sun, *J. Am. Chem. Soc.*, 2016, **138**, 14546.
42 H. Zhang, S. Hwang, M. Wang, Z. Feng, S. Karakalos, L. Luo, Z. Qiao, X. Xie, C. Wang, D. Su, Y. Shao and G. Wu, *J. Am. Chem. Soc.*, 2017, **139**, 14143.
43 J. Yin, Y. Li, F. Lv, Q. Fan, Y. Q. Zhao, Q. Zhang, W. Wang, F. Cheng, P. Xi and S. Guo, *ACS Nano*, 2017, **11**, 2275.
44 L. Wang, W. Zhang, X. Zheng, Y. Chen, W. Wu, J. Qiu, X. Zhao, X. Zhao, Y. Dai and J. Zeng, *Nat. Energy*, 2017, **2**, 869.
45 T.-H. Shen, L. Spillane, J. Vavra, T. H. M. Pham, J. Peng, Y. Shao-Horn and V. Tileli, *J. Am. Chem. Soc.*, 2020, **142**, 15876.
46 W. Sohn, K. C. Kwon, J. M. Suh, T. H. Lee, K. C. Roh and H. W. Jang, *Nano Convergence*, 2021, **8**, 11.
47 K. Urita, T. Fujimori, H. Notohara and I. Moriguchi, *ACS Appl. Energy Mater.*, 2018, **1**, 807.
48 W. Wang, J. Jiang, T. Ding, C. Wang, J. Zuo and Q. Yang, *ACS Appl. Mater. Interfaces*, 2015, **7**, 2235.
49 U. I. Kramm, M. Lefevre, N. Larouche, D. Schmeisser and J. P. Dodelet, *J. Am. Chem. Soc.*, 2014, **136**, 978.
50 M. W. Louie and A. T. Bell, *J. Am. Chem. Soc.*, 2013, **135**, 12329.

51 B. S. Yeo and A. T. Bell, *J. Am. Chem. Soc.*, 2011, **133**, 5587.
52 A. Moysiadou, S. Lee, C.-S. Hsu, H. M. Chen and X. Hu, *J. Am. Chem. Soc.*, 2020, **142**, 11901.
53 N. Kornienko, J. Resasco, N. Becknell, C.-M. Jiang, Y.-S. Liu, K. Nie, X. Sun, J. Guo, S. R. Leone and P. Yang, *J. Am. Chem. Soc.*, 2015, **137**, 7448.